nature communications

Article

https://doi.org/10.1038/s41467-025-61838-3

Field-programmable robotic folding sheet

Received: 31 January 2025

Accepted: 30 June 2025

Published online: 05 August 2025

Check for updates

Hyunkyu Park[1,6], Yongrok Jeong[2,6], Woojong Kim[1], Jungrak Choi[3], Junseong Ahn[4], Jun-Ho Jeong[5], Inkyu Park[1] ✉ & Jung Kim[1] ✉

Shape transformation by folding showcases intricate geometrical change over dimension, that has long provided the embodied intelligence of autonomous systems capable of adapting to challenging environments and displaying functional versatilities. Hinge-face material assembly interfaced by shape-morphing mechanisms produced the associated means. However, the fixed hinge structure limits the accessible modes of folding configurations despite the existing capability of rectification in plant. Here we introduce a programming strategy of the two-dimensional fold of a robotic sheet into an unbounded set of hinge configurations in the field post-deployment, which is referred to as being field-programmable, driven by a densely distributed electro-thermo-responsive system design. An interconnected set of metallic resistors, incorporated into the thermo-responsive polymer film, performs the dual functionalities of a heater and thermoreceptor, selectively recruited to configure folds through electronic modulation of its electrical power distribution. Electronic layouts, computational algorithms, and closed-loop control schemes present an intuitive means of blending user intent in situ, yielding a servoed, swift, and robust fold-programming process. The system is intrinsically driven by embeddable electronics to enable autonomous system engineering, as potentiated by multi-purpose applications in grasping and locomotion.

Shape-transformable device design holds promise for future robotic system facing dexterous interaction with surroundings in a variety of domains[1,2], such as exploration[3–7], conformable manipulation[8], deformable electronics[9], haptic display[10], and smart healthcare[11]. Shape-morphing mechanisms using soft materials that are responsive to various external stimuli (using magnetic[12–15], electrical[16–18], optical[19,20], chemical[21,22], fluidic[23–25] interactions) harness intricate shape changes that conform to a range of scale (from micro-[11,26] to meso-[12,22], macro-[24,27] scale), endure environmental extremities (underwater[28], debris[29], and aerospace[30]), and serve distinctive functions on demand (e.g., remoteness[31], damage resilience[32], and biocompatibility[33]), that are challenging to achieve with traditional rigid components. Advancements in material assembly technology[8,27,34] and computational shape prediction strategy[35,36] facilitate delicate design of shape-morphing process. For instance, shape morphing by folding has been programmed on a planar scratch using the spatial distribution of folding[27] or local bending[37,38] actuations, often in the form of hinge-face assemblies[39]. However, the predetermined shape configurations would permit limited configurations of accessible shape modes that are irreversible, or in-plant rectifiable[26,27,40–43]. Therefore, the future of autonomous deployment of the associated systems lies in a dynamic, in-place programmable (or, field-programmable) shape-morphing process that copes with varying user intents. The resulting inspiration drawn from the evolutionary trajectory of display engineering and programmable logic devices invites a distributed material architecture integrated with a spatially addressable control scheme, which involves a pixelated hardware design adopting different display-addressing schemes (direct

[1]Department of Mechanical Engineering, Korea Advanced Institute of Science and Technology, Daejeon, Republic of Korea. [2]School of Mechanical Engineering, Kyungpook National University, Daegu, Republic of Korea. [3]Electronics and Telecommunications Research Institute (ETRI), Daejeon, Republic of Korea. [4]Department of Control and Instrumentation Engineering, Korea University, Sejong, Republic of Korea. [5]Korea Institute of Machinery and Materials (KIMM), Daejeon, Republic of Korea. [6]These authors contributed equally: Hyunkyu Park, Yongrok Jeong. ✉e-mail: inkyu@kaist.ac.kr; jungkim@kaist.ac.kr

addressing[10,44], and matrix addressing[45]) and a networked domain driven by periphery electrodal stimulation[46–48]. Despite significant progress, the field-programmability for folding has remained uncharted, which would form the basis for the design space of autonomous robotic systems[39]. To this end, the following challenges are of concern. (i) The hinge should be digitally reconfigurable with densely distributed stimulation segments, offering sufficient spatial resolution and number of degrees of freedom in the shape-programming process. (ii) The curvature inducement should be maneuverable, providing a sufficient range of shape change, at least covering a folding angle of −90 ° to 90 °. (iii) Eliminating the reliance on extrinsic driving principles that confine operations to fixed workspaces. (iv) The need for internal sensing modalities to monitor drive state, in order to servo, accelerate, and robustify the shape-morphing process (see Supplementary Note 1 and Supplementary Table 1 for detailed explanation about contribution of our work).

Given the requirements, we demonstrate a robotic folding sheet whose region, direction, and degree of change are field-programmable using an electrothermal shape-morphing mechanism that is two-dimensionally distributed, spatially selective, thermoceptive, and closed-loop controlled (Supplementary Movie 1). The use of electrical driving principle provides a means of intrinsic operation using embeddable electronics, facilitating the exterior autonomous operations (see Supplementary Note 2 for details on the selection of driving principle). A functional basis of the robotic sheet incorporates a distributed set of networked metallic resistors, each of which serves as both heater (as per the Ohmic heating principle) and thermoceptor (through its resistance which is $\propto \alpha \Delta T$, where α is a temperature coefficient, and T is temperature) (Fig. 1a). The folding region, or hinge, is digitally reconfigurable by redistribution of electrical power among the resistor segments through the dense electrode connections (Fig. 1b(i)). Given the thermal inducement, a thermo-responsive shape-morphing structure, which encapsulates the resistive network, induces large, fast, and spatially uniform folding deformation in a bidirectional manner, driven by relative heating and passive cooling from the temperature for structural neutralization. The temperature state is measured in situ based on the distribution of the resistance changes, exploiting the interconnected regime associated with the numerical reconstruction scheme, referred to as resistive network imaging (RNI) (Fig. 1b(ii)). The integrated operation of the functionalities serves as a perquisite of closed-loop control of temperature, without adding further complexity to the hardware design, being solely driven by electronically programmable logics with fast functional transition (< 1 μs) while avoiding mutual interference (due to their large differences in electrical power level, that is $\propto I^2$, where I is the current ranging approximately 200 mA; actuation, <2 mA; sensing, for each electrode).

The resulting programming process of fold displays rich reconfigurability under user guidance. Many opportunities exist to adjust the folding region that can be translated (Fig. 1c(i)), rotated (Fig. 1c(ii)), and accumulated to achieve bending (Fig. 1c(iii)), while managing the directionality of each folding (Fig. 1c(iv)). Based on these capabilities, several complicated shapes can be produced, provided the zero Gaussian curvature is preserved, such as a wavy pattern (Fig. 1d), multifold with diverse orientations (Fig. 1e), and rolling by large range of bending (Fig. 1f). Associated investigations, which include finite element analysis (Fig. 1g(i)), and temperature measurements (using infrared camera (Fig. 1g(ii)), and RNI estimation (Fig. 1g(iii))) promote a deeper understanding of the fold-programming process.

Results

The design of the functional basis, which includes the resistive network geometry and electrode arrangement, is the first step toward achieving a high degree of freedom in accessible shape configurations. The building block of the resistive network geometry takes the form of a centered square lattice containing four auxiliary resistors interconnected at the center of the unit lattice. The unit structure closely

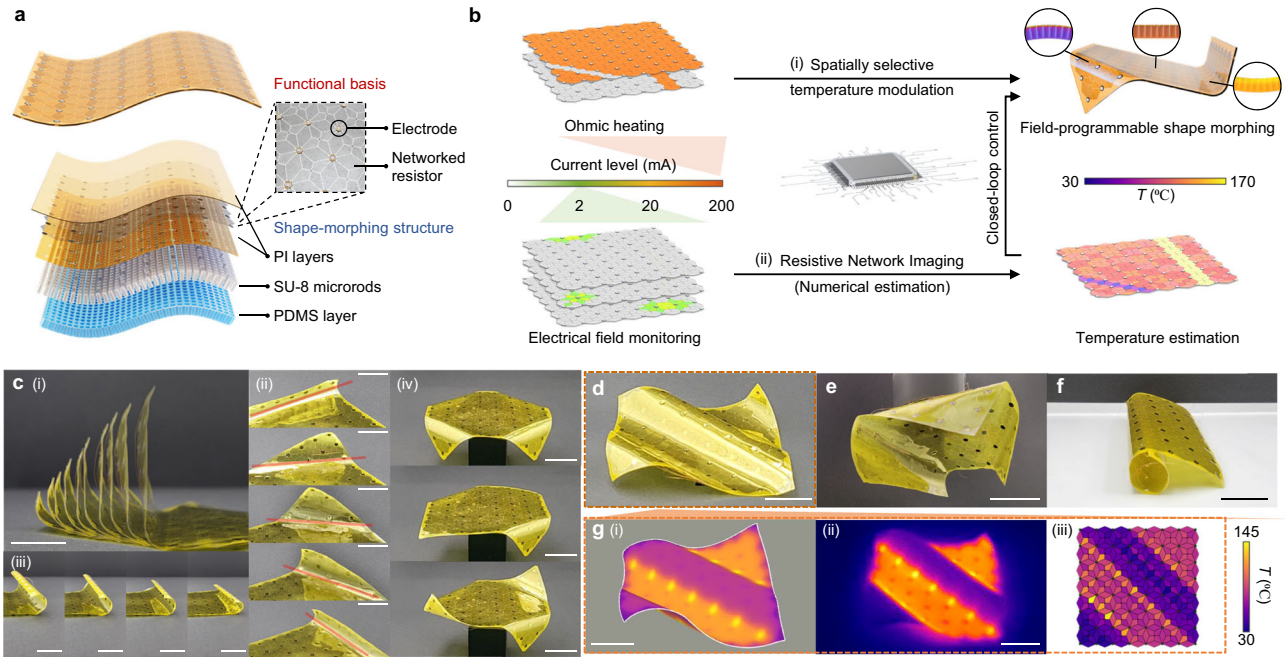


Fig. 1 | Field-programmable robotic folding sheet. a Schematic illustration of a material architecture composed of the functional basis and the shape-morphing structure. The geometries of the microstructured components (SU-8 microrods and PDMS) are enlarged, for clarity. **b** Schematic illustration of a computational architecture that drives (i), senses (ii), and thereby closed-loop controls the temperature (T) distribution to program thermo-responsive folding. **c** Demonstration of field-programmability in folding, exemplified by folding region being translated (i), rotated (ii), and accumulated to achieve bending (iii), along with maneuvering fold directionality (iv). For c(ii), red line indicates the principal axis of fold. Scale bars, 15 mm. **d**–**f** The high degree of freedom in shape-programming process can display a complicated form of shape as a wavy pattern (**d**), multifold with diverse orientations (**e**), and rolling (**f**). Scale bars, 15 mm. **g** Investigations on the shape-programming process, using Finite element analysis (i), infrared camera measurement (ii), and RNI temperature estimation (iii). Scale bars, 15 mm.

resembles the box-pleated origami pattern, which can serve as a universal shape approximator with its flexible arrangement[27,39,49–51]. The robotic sheet presented here adopts a 7 × 7 grid arrangement of 0.9 × 0.9 cm unit blocks to form a 6.3 × 6.3 cm square, embedding total 308 resistors. An electrode arrangement is applied to the vertex of each lattice, resulting in an 8 × 8 grid configuration. A contrary domain design would involve a pixelated approach, which has long served as a basis of generic distributed information processing. A singular value analysis on the outcoming electrical power distribution supports the fact that the use of such a networked domain is better suited for folding, which stems from an orchestrated result of a set of segmental deformations, thereby gaining greater benefits by finer domain subdivision (number of segments exceeding the number of electrodes) despite the loss of individual addressability of resistors (see Supplementary Fig. 1, "Methods"). The realization of the networked resistor is tailored by a careful selection of geometry in the form of a serpentine shape to achieve spatial uniformity in heating, packed into a kite geometry to ensure complete surface occupancy when arranged (Supplementary Note 3 and Supplementary Fig. 2). The governing geometrical parameters in the shape are tuned to suppress the effect of parasitic resistances in the electronics, by ensuring factor of 9 to the resistance level. The electrode connection is established by soldering ultra-thin wires (diameter of 50 μm (AWG 45)) to reduce mechanical interference caused by tension.

The electrothermal shape-morphing mechanism involves a bilayered structure, imparting a mismatch in thermal expansion. Among various set of materials, a stack of Polyimide (PI) and Polydimethylsiloxane (PDMS) can offer a large curvature response (coefficient of thermal expansion $\alpha = 45$, 340 ppm/K, respectively). The proposed robotic sheet further adopts a microstructuring technique to enhance mechanical performance. Grid-arranged rigid microrods (SU-8) are reinforced with PDMS in an out-of-plane direction, resulting in desirable transverse isotropy in the thermal expansion by enhancing the lateral thermal strain in response to restricting medial mechanics. Microscopic finite element analysis and specimen test validates the mechanism in comparison with the monolithic design (Supplementary Figs. 3, 4). Moreover, the microrod structure enhances the mechanical durability of the sheet by interlocking PDMS with PI, which possess low adhesion properties (Supplementary Fig. 5). A precise fabrication of the SU-8 microrod is performed by lithography, covered with PDMS. We refer to Methods and Supplementary Fig. 6–8 for fabrication, and Supplementary Note 4 for point-by-point instructions on the fabrication protocol for reproducibility. The use of PDMS presents a simple means of tuning the curvature range by adjusting the curing temperature T_c. The experimental result indicates the high linearity in the relationship between T_c and temperature for structural neutralization $T_{\kappa=0}$, the value for our demonstration which was set as 100 °C (equivalent to $T_c = 120$ °C) to achieve a symmetric bi-directionality within the operation range of 30–170 °C (upper-bounded by long-term PDMS denaturalization) (Supplementary Fig. 4). Many opportunities exist to tune the curvature range according to a particular application scenario.

Spatial locality in physical response (both the thermal and mechanical) serves as the basis for spatial resolution in the fold-programming process. Our electrothermal stimulation results in a spatially concentrated temperature response, regardless of the variance in resistor recruitment strategies (Fig. 2a). We attribute this thermal locality to the thin-filmed geometry, which enforces the dominance of convection over internal heat accumulation. To further investigate the resulting mechanical response, which is difficult to measure in a distributional form, whole-body-scale finite element analysis was conducted (Fig. 2b). The overall sheet structure is discretized into a multi-layered shell element while approximating the microscopic details in PDMS/SU-8 composite into a monolithic component using the rule of mixture, to mitigate excessive computational costs. The computation emulates a vertical line-folding scenario using properly assigned inlet electrical energy distribution. In coherence with the temperature response, which shows a good agreement with the experimental measurements, the mechanical responses (von Mises. Stress and maximal principal strain) exhibit considerable spatial locality (Supplementary Fig. 9). The results facilitate straightforward calibration by configuring the shape solely in units of segmental resistor occupancy.

Experimental studies present the detailed features of the folding. Under identical folding configurations as in the whole-body simulation, the folding exhibits a large average curvature change in both directions, ranging from −1.80 cm^{-1} to 2.11 cm^{-1}, corresponding to the overall folding angle from −87° to 109° (Fig. 2c). Benchmarks from previous studies demonstrate the considerable morphing performance of our material design, despite its multi-directionality in folding (Supplementary Note 5, Supplementary Fig. 10, and Supplementary Table 2). A curvature distribution analysis reveals the noteworthy locality of deformation inducement, as 82.8 ± 6.80 % of the curvature is concentrated in the stimulated region (Fig. 2d). This result shows a good agreement with the locality of the simulated thermomechanical response. At the peak of the curvature distribution, high linearity is observed with respect to temperature changes ($R^2 = 0.932$). We attribute this linearity to careful material selection ensuring consistent mechanical properties within the governing range of strain changes (< 0.5 mm/mm). The folding at various regions is revealed as consistent, overall adhering to the range of 1.35 ± 0.20 cm^{-1} (Fig. 2e). Enhancing repeatability is crucial in thermo-responsive folding mechanisms, given the tendency for delamination within layered structures. The folding in our sheet withstands repeated operation, as investigated by 1000 repeated cycles of toggling at 0.05 Hz (absolute value of slope < 10^{-5}, $|R^2| > 0.95$) (Fig. 2f). This reliability is attributed to enhanced material adhesion facilitated by the microstructuring. The performance is consistent along the fabrication variations (Supplementary Fig. 11).

The field-programming of folding is equivalent to modulating the temperature distribution upon the user guidance, referred to as a morphing command ($\Delta\mathbf{T}_c \in [0, 140]^M$ °C, where M is the number of resistors), that may be decided by intuition or computational shape prediction (Fig. 3a). A desire for flexible recruitment of multiple folding indications invites a segmented modulation strategy for configurations of each folding, which involve a region of folding and a degree of change. To this end, the morphing command is decomposed to the set of isolevel morphing intents, separately modulated in a stackable, sequential manner (Fig. 3a(i)). Pulse-width modulation (PWM) scheme drives the stack of the modular intents. Each of the intents can be represented as a joint of morphing basis ($\in [0, 1]^M$), a binary indication of the segmented region, and morphing rate ($\in [0, 100]$%, a ratio to maximal temperature change of 70 °C) governing the desired temperature change. Electronic operation casts the morphing basis imposition as a pulse, through a temporally configurable toggling (that refers to the duty cycle) of the suitable electrodal voltage set, selected within the fixed levels (−15, −10,… 15 V) for simplicity in circuit logic (Fig. 3b).

Genetic algorithm is employed for accurate and reliable electrodal voltage prediction, to address the high nonconvexity and nonlinearity in the associated relationship (see "Methods"). Precisely tuned configurations achieve a good convergence through iteration, high accuracy, and fast operation (completion in <0.8 s, capable of parallel computation on morphing bases) (Supplementary Fig. 12). Given the prescribed variables, fast and linear electrothermal response using duty cycle control facilitates reliable temperature modulation. The time period of the pulse is carefully selected as 8 ms to balance the system bandwidth and power efficiency (Supplementary Fig. 13a). The resulting temperature change from duty cycle control exhibits high linearity ($R^2 > 0.993$), providing a reliable means to calibrate the duty

https://doi.org/10.1038/s41467-025-61838-3

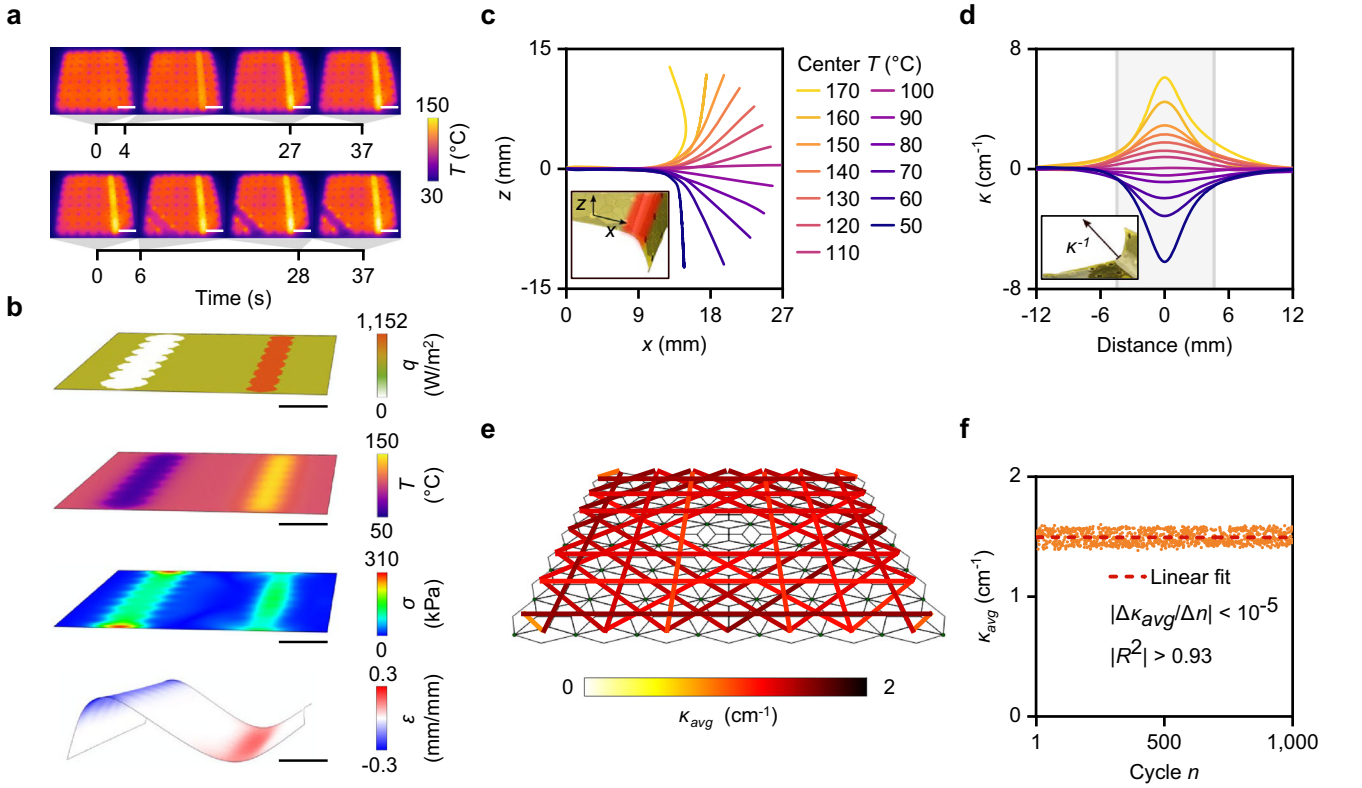


Fig. 2 | Numerical and experimental investigations of the folding principle. **a** Electrothermal stimulation exhibits spatially localized response of temperature T. Scale bars, 15 mm. **b** Whole-body FEA prediction on the dual, apposite vertical folding configuration. The multi-physical computation displays spatially localized response of temperature T, von Mises stress σ, and maximum principal strain ε, with respect to inlet energy q. Scale bars, 15 mm. **c** Contours traced along the edge when folded in response to temperature variations represented by its center value. The inset shows a photograph of the applied folding configuration (stimulated region depicted in red), along with graphical illustration of the associated coordinate system (x-, z-axis). **d** The curvature (κ) distribution of the contours shown in (**c**). The inset shows the graphical illustration for defining curvature κ. The gray box represents the region of activation. **e** Spatial consistency of folding response in various folding configurations. Each line represents the region of folding, with the color indicating the value of κ_{avg}, curvature averaged along the deformed curve, resulting from the consistent inlet energy density stimulation. **f** Folding response to 1000 cycles (n) of toggled stimulation inducing a folding configuration identical to (**c, d**).

cycle to the morphing rate (Supplementary Fig. 13b, c). A dynamical behavior due to the pulsed operation, represented as a time constant, displays a tolerable lag (Supplementary Fig. 13d), in comparison with a plain response from invariant voltage stimulation (Supplementary Fig. 13e, f).

The thermoception through resistance changes enables intrinsic monitoring of the temperature state in our sheet. The RNI presented here stems from Electrical impedance tomography (EIT) technology, which has served as a means for measuring the resistance distribution[52] (Supplementary Fig. 14; see "Methods"). The method is a definite alternative to infrared camera measurement, which is vulnerable to visual occlusion due to folding and has limited utility in exterior applications. The invariance in temperature coefficient of the metal ($\alpha = 0.006$/K for Ni) offers straightforward calibration of RNI result to temperature. The RNI operation involves the investigation of the electrical potential distribution by the patterned, and repetitive recruitment of electrode pairs for current injection and voltage measurement. Thereafter, a numerical inverse computation process is used to reconstruct the distributed thermo-responsive resistance changes (Fig. 3c). Given the high accuracy of the electrical simulation (Supplementary Fig. 14a), we leveraged a deep learning-based reconstruction method with a sim-to-real transfer approach[53] to establish fast, accurate, spatially uniform, and well-generalized measurement (Supplementary Fig. 14b, c, Supplementary Fig. 15, Supplementary Movie 2).

Delicate scheduling and the compact drive electronics based on a field-programmable gate array (FPGA) ensures fast integrated operation of these functionalities, lasting approximately 8 ms per morphing basis for actuation and 15 ms per frame for sensing (Supplementary Figs. 16, 17). For each morphing basis recruitment, proportional-integral (PI) control was performed on the duty cycle (Fig. 3a(ii)). The segmental temperature estimation for each morphing basis (aggregated upon the region of interest) is performed by non-overlapping attention to the temperature measurement (Fig. 3a(iii)).

The resulting demonstration showcases a dynamic shape reproduction in response to the temporal progression of user intent (Fig. 3d, Supplementary Fig. 18a and Supplementary Movie 3), The set of morphing bases is flexibly recruited with varying morphing rates to individually and continuously handle the degree of each folding (or, bending). The curvature response to the duty cycle displays high linearity ($R^2 > 0.95$) in the steady state across the various morphing basis recruitments (Fig. 4a). The closed-loop control strategy presents accurate servoing of temperature, and thereby of curvature (Supplementary Fig. 18b). The control performance is characterized using frequency response analysis. Figure 4b presents a sample trajectory tracking result of the harmonic reference signal (0.09 Hz). The nonlinearity in system dynamics arises from asymmetry of the heat transfer process. Peak-to-peak and cross-correlation analyses are devised for measuring the magnitude and phase, respectively, in such a nonlinear system. In both the temperature and curvature, the system bandwidth is improved from <0.03 Hz when uncontrolled to approximately 0.1 Hz when closed-loop controlled (Fig. 4c). The phase shift shows good agreement with the observation in magnitude, exhibiting reduced phase shift of approximately -85^0 to -55^0 at the bandwidth (Fig. 4d). A transient response analysis supports these improvements in control performance, especially in terms of settling

https://doi.org/10.1038/s41467-025-61838-3

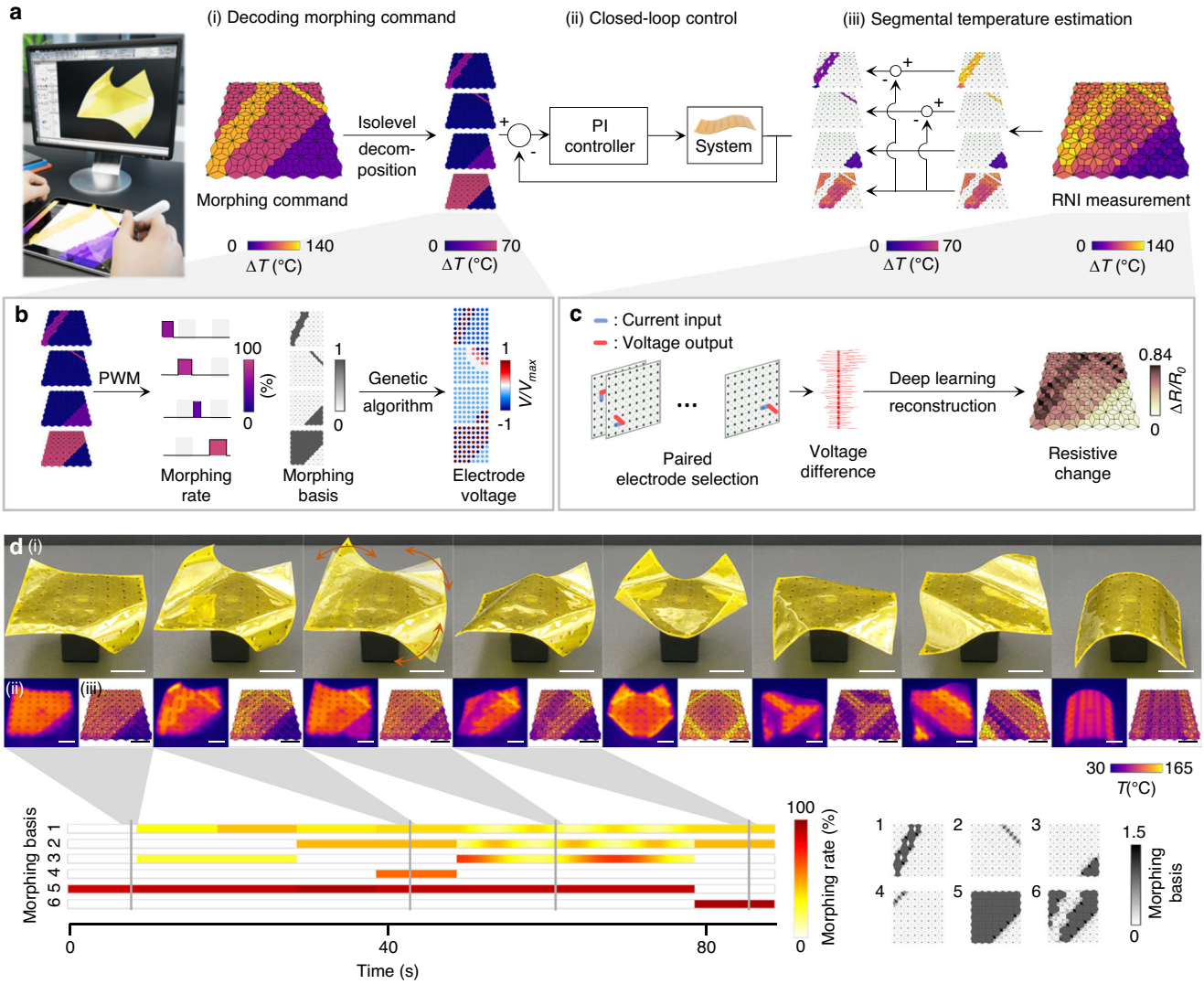


Fig. 3 | Programming and control of the folding process. a Computational pipeline of shape-programming process by control of temperature (T) distribution. The first step involves decoding of the morphing command into the set of modularized variables (i). Proportional-integral (PI) control on the morphing instruction modulates the temperature distribution (ii), based on the RNI temperature measurement (iii). **b** Schematic illustration of pulse-width-modulation (PWM)-based morphing basis recruitment. Genetic algorithm decodes the morphing bases into the set of electrodal voltage V that is normalized by maximum voltage level V_{max}. **c** Schematic illustration of the driving principle of the RNI-based temperature measurement. Resistive changes ΔR (normalized by base level R_0) are reconstructed. **d** Demonstration of dynamic shape-programming process in response to sequential user intents, with a photograph of sheet operation (i), IR camera image (ii) and RNI temperature estimation (iii). The below inset shows the schematic illustration for the temporal flow of morphing basis recruitment within a selected morphing scenario. The morphing bases decoded by genetic algorithm are presented. (For the data on the rest morphing scenarios, see Supplementary Fig. 18a). Scale bars, 15 mm.

time and steady-state error (Supplementary Fig. 19). The required power consumption for the morphing scenario presented in Fig. 3d is shown in Supplementary Fig. 18b, displaying a lumped power-to-heat conversion efficiency of 12.59 %.

In practice, the robotic sheet may encounter undesirable thermal disturbances, such as winds and varying ambient temperature (Fig. 4e, f, Supplementary Movie 4). The proposed controlled shape morphing can retain the temperature and shape under both surrounding conditions. In contrast, open-loop control exhibits shortcomings, being underactuated under the influence of winds that accelerate air convection and overactuated when subjected to elevated ambient temperatures.

The diverse features of the proposed robotic sheet enable the development of intelligently engineered components, whose functionality is dynamically reprogrammable post-deployment upon shape change. As a proof of concept, we demonstrate a compelling application scenario for an extraterrestrial exploration rover that would require multi-purpose operation with a streamlined hardware design (Fig. 5a). Soft robotic grippers have been extensively explored as an alternative to rigid construction, to provide a gentle, conformable physical interaction with fragile or unknown objects, organisms, and surroundings[54]. Grasping with this robotic sheet further advances the associated object manipulation strategy by dynamically adjusting the grasping pose within commonly used hardware (Fig. 5b, Supplementary Movie 5). For instance, multi-pod grasps, winding, pinch, or wrap can be programmed online and on-demand to fit into various object topologies (Supplementary Fig. 20a) while achieving a maximum payload-to-weight ratio of four, which is adequate given the thin-film structure (Fig. 5c, Supplementary Fig. 21). We anticipate the enhanced practicality of relevant future gripper designs through design customization and utilization of diverse surface adhesion techniques[55].

https://doi.org/10.1038/s41467-025-61838-3

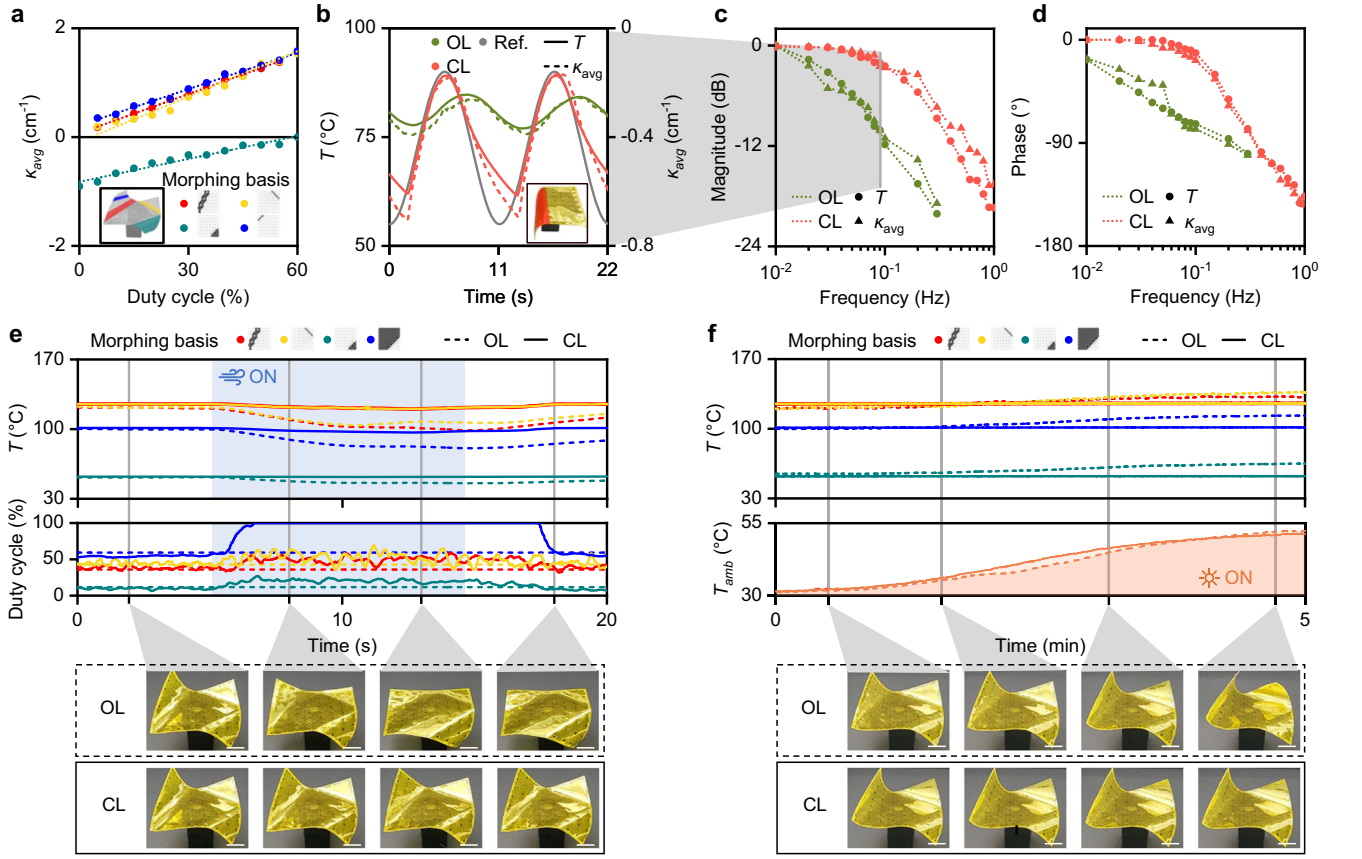


Fig. 4 | Closed-loop control servos, accelerates, and robustifies the folding process. a Averaged curvature (κ_{avg}) response to duty cycle modulation. Morphing bases {1, 2, 3, 4}, indexed in Fig. 3d, are adopted for the experiment, under recruiting the morphing basis 5 as the role of flattening. Dashed lines indicate linear fit (all show $R^2 > 0.95$). The inset shows the region of folding by each morphing basis recruitment. **b** A trajectory tracking 0.09 Hz harmonic temperature input T. The inset shows a photograph of the applied folding configuration (activated region is depicted in red). **c, d** Frequency response in temperature control, in magnitude (**c**) and phase (**d**). Same shape configuration is adopted as (**b**). **e, f** Demonstration of thermal robustness to wind (**e**) and changes in ambient temperature T_{amb} (**f**). The shape configuration adopts the set of morphing bases {1, 2, 3, 5} indexed in Fig. 3d. The insets show photographs of the sheet operation. Scale bars, 15 mm. For (**b**–**f**) OL and CL denote open-loop control and closed-loop control, respectively.

Robotic exploration in challenging terrains (rugged and obscured) may require a compact system design and the ability to perform dexterous locomotion that can benefit from robotic designs with structural compliance. The field-programmability presented here expands the available modes of locomotive strategies. For instance, when the robotic sheet is deployed on the ground, the robotic sheet can imitate various bio-inspired movements such as crawling, waving, walking, and dragging (Fig. 5d, Supplementary Movie 6). Delicate scheduling of sequential morphing basis recruitment (Supplementary Fig. 20b) and closed-loop temperature control produces movements of up to 26.44, 8.85, 6.27, and 9.80 mm per stroke for each locomotion (Fig. 5e). In the future, an automated computational framework with dynamic simulations may be used to promote an optimized shape-morphing strategy adaptive to terrain conditions[56].

Discussion

In conclusion, the proposed robotic sheet demonstrates shape morphing by folding that is programmable in the field upon dynamic interaction with users. The integration of advances in materials, computation, and electronics facilitates the delicate maneuvering of numerous shape configurations that alleviate the use of fixed hinges as in previous attempts. A servoed, swift, and robust morphing of the shape through intrinsic modalities of actuating and sensing, and thus closed-loop control of the temperature distribution, presents many opportunities for deployment in diverse exterior autonomous robotic systems, as potentiated with our multi-purpose grasping and locomotion.

Despite these promising features, several concerns should be addressed to further mature our technology. First, the mechanical performance should be improved to enhance both shape responsiveness and load-bearing capacity. Additional material advancements should be investigated beyond our micro-rod structure, including thermo-responsive meta-materials that outperform conventional materials[57], or a structural design with a thicker form factor that would require accelerated cooling mechanisms[58,59]. Such modifications would enable a more complex folding process featuring overlapping or curved folds. Second, the practical applications of the robotic sheet should be explored in greater depth, including potential demonstrations as a light modulator[47] or a dexterous robotic platform for environmental monitoring[60]. To this end, the replacement of wire-based interconnections to in-hardware electrode traces and the straightforward insertion of add-on elements, such as intrinsic shape sensing modalities, should be further investigated. Furthermore, the demonstration of generalized shape programmability with various form factors would extend the effectiveness of our framework that would incorporate the flexible assembly of unit elements across scales and dimensions. All these efforts would expand the scope of versatile engineering methodologies by blending intelligence in morphology and computation.

https://doi.org/10.1038/s41467-025-61838-3

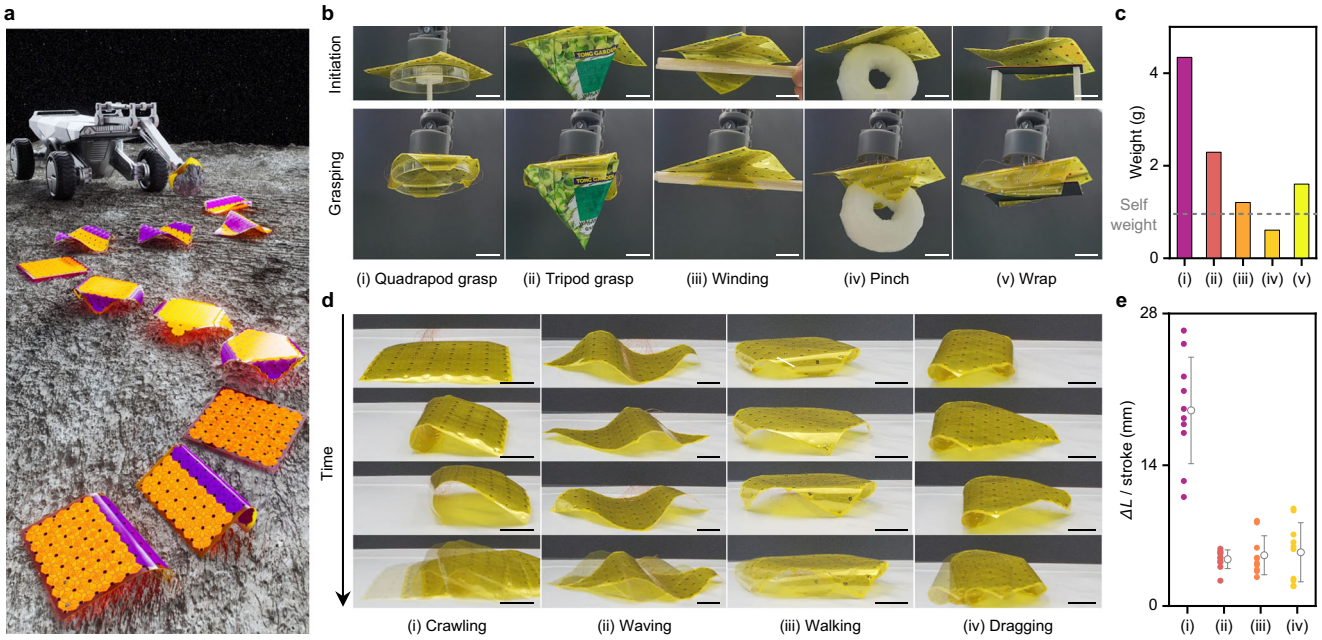


Fig. 5 | Applications of the robotic folding sheet. a Schematic illustration of multifunctional operation in the extraterrestrial rover. **b** Shape-adaptive grasping of object with varying topology. For each scenario, the top photograph shows the initiation of the grasping, while the photograph below demonstrates the completion of grasping. **c** Object weight in the grasping. The self-weight of the sheet is shown as a gray dashed line. **d** Demonstration of the selected locomotive strategies. From top to bottom, three snapshots are presented to display the sequential changes in the shape, while the last photograph captures the three strokes at once to highlight the displacement. **e** Locomotive performance evaluation by measuring displacement ΔL for each of the ten strokes. Error bars, mean ± s.d.

Methods

Functional basis

The arrangement of the resistors and electrodes forms a substantial basis for distributed domain design. The proposed networked resistor, consisting of a centered square lattice, was proposed as an alternative to pixelated strategies to facilitate a higher degree of freedom in distributional temperature programmability, given an identical number of electrodes. The degree of the individual addressability can be evaluated in terms of the independence of the power output of each resistor segment. Given a set of feasible electrical power distributions, the uniformity of the singular value distribution represents the associated means. To this end, the singular value distribution of the set of possible outcomes (electrical power distributions under a fixed electrodal voltage value {−1,0,1} V) was investigated and compared with a range of resistor designs, including those in the pixelated and networked domains characterized by electrode arrangement (ports only at the periphery and uniform grid ports) and resistor network configuration (with or without interconnection at the center) (see Supplementary Fig. 1 for the result of singular value analysis). The results indicate that our design contains a larger number of significant singular values (above the sharp drop in the value) than the other networked domains. Pixelated domains guarantee definite independence in resistor control, but the sample demonstration of the line folding scenario further confirms that there is a better chance for our networked design to enrich the available folding configurations (example cases of comparison are shown in Supplementary Fig. 22). A distributional variance analysis further supports the outperformance of the networked domain (see Supplementary Note 6 and Supplementary Fig. 23). The geometry of the serpentine resistor was designed to achieve spatial uniformity in thermal power density throughout the surface (See Supplementary Note 3 for details on the design of the resistor geometry).

Fabrication

The networked resistor is a functional layer of nickel (150 nm) with an adhesive layer of chromium (3 nm), and was fabricated using a lift-off process on a spin-coated PI substrate. A Cr/Al etch-stop layer was then deposited with a shadow mask. The fabricated networked resistor was covered with an additional PI layer for insulation and protection from the external environment. An additional Al layer was fabricated on the encapsulated network resistor film using the lift-off process. By adopting both the upper and lower Al layers as the etch-stop layers, a via hole was formed via reactive ion etching (RIE). Subsequently, the Al layer was wet-etched. To address the poor solder wettability of Ni, a solder-wetting layer (Cr/Cu/Au) was deposited with a shadow mask on the fabricated via holes. Subsequently, the SU-8 microrod pattern was formed by lithography and then hard baked. A solder pad was then formed at the via hole via cream soldering. On the overall layer, PDMS was spin-coated and cured at the temperature of T_c. Subsequently, the PDMS over the solder pad was scraped, and the fabricated sheet was delaminated from the wafer. The fabrication process was completed by attaching an ultrathin electrical wire (45 AWG) via soldering. (See Supplementary Note 4 and Supplementary Figs. 6–8 for details of the fabrication protocol).

Finite element analysis

Microscopic simulation. The set of components constituting each material was separately constructed to mimic part of the sheet structure (occupying an area of 975 × 975 μm) using solid geometry and tetrahedral meshing (ABAQUS/CAE 6.14; Dassault Systèmes, France). Each component was assembled with a tie constraint at its interface. The metallic resistor layer was approximated as a monolithic component for computational simplicity. Instantaneous uniform surface heat flux was imposed on the metal layer, with the value achieving maximum temperature elevation ($\Delta T = 70$ °C) over the structure at steady state. The center fixation at the bottom served as a mechanical constraint for shape change. Natural air convection with a coefficient of 3.6 W/m^2 · K (on the outermost and innermost faces) and geometrical nonlinearity was implemented. (See Supplementary Table 3 for the material properties used in the simulation).

Whole-body simulation. The computation approximated the sheet as a 4-node composite shell with three integration points for each layer (ABAQUS/CAE 6.14; Dassault Systèmes, France). As in the microscopic computation, the electrothermal stimulation of each serpentine resistor was approximated as an instantaneous uniform surface heat flux, which was estimated using Joule's first law for each segment. The thermal and mechanical properties of the PDMS/SU-8 shell composite were integrated to form a single reinforced laminate based on the rule of mixture by assuming linearity in the elasticity of PDMS and considering its moderate strain range (< 0.5 mm/mm). As in the microscopic simulation, identical configurations of mechanical constraints, air convection, and geometrical nonlinearity were implemented; the material properties are listed in Supplementary Table 3.

Characterization experiments on folding principle

Relationship between T_c and $T_{\kappa=0}$. The samples prepared for the experiment had the same structure as the robotic sheet, occupying three networked resistor lattices in a line (9 × 27 mm). The end of the lattice was tapered using commercial PI tape to enforce unidirectional bending; otherwise, the energy is dissipated to the nonprincipal axis owing to the transversely isotropic thermal expansion of the materials. Four samples were prepared with different PDMS curing temperatures (T_c = 90, 120, 150, 180 °C, respectively). To measure the temperature responses of the fabricated samples, the test was conducted in a convection oven (LCZ1402; Lacuzin, South Korea) to ensure uniform heating. The temperature was measured using a thermocouple (Type K ST-5; RKC Instruments, Japan, logged using a LOGGER GL220; Graphtec Corporation, Japan) attached to the sample, and the corresponding curvature of the central unit cell was estimated using camera image analysis.

Temperature distribution measurement. An infrared thermal camera (TE-Q1; i3 systems, South Korea) was used to measure the temperature distribution throughout the sheet. The images were further processed by pixel-level analysis using MATLAB (MathWorks, USA) and T.E Analyst software (i3 systems, South Korea).

Thermodynamical response. The thermodynamical response was measured by substituting the thermal camera, having low temporal resolution (frame rate of <10 Hz), with a film-type customized resistance temperature detector (RTD) capable of ultrafast analog acquisition with the help of FPGA-mediated electronics (sampling rate of 10 kHz). Following a similar fabrication process as that of the robotic sheet, the RTD of size 6.3 × 6.3 mm and thickness of 15 μm was fabricated as per the design illustrated in Supplementary Fig. 24. Data processing was performed using digital low-pass filters with an appropriate cutoff frequency (100 Hz).

Distributed actuation

The presented distributed actuation presented aims to modulate the temperature distribution using specific strategies for the intuitive handling of user intents. Given M number of resistors, the user intent on target distribution of temperature change, defined as a morphing command $\Delta\mathbf{T}_c \in [0, 140]^M$ °C, was modularized into a set of morphing bases $\mathbf{X}_i \in \{0,1\}^M (i \le 4)$, and morphing rate $w_i \in [0, 100]$%. The number of maximal morphing basis recruitments (four in this work) was empirically selected as a compromise between system bandwidth and control capacity. The value of the morphing rate is equivalent to the increase in desired temperature of intent, scaled by the maximum change of temperature (70 °C) for structural neutralization. Decomposition was performed by compartmentalizing the folding region guided by the user, which may form an isolevel for simplicity. The overall decomposition could be expressed as $\Delta\mathbf{T_c} = 0.7\sum_{i=1}^{4} w_i \mathbf{X}_i$.

The forward problem in the decoding of morphing basis relates the electrode voltage configurations $\mathbf{A} \in \mathbb{R}^N$, N is the number of electrodes, to the electrical power distribution $\mathbf{E} \in \mathbb{R}^M$ throughout the resistive network $\mathbf{R} \in \mathbb{R}^M$. Using Kirchhoff's current law, electrical current distribution $\mathbf{I} \in \mathbb{R}^M$ can be estimated by

$$\mathbf{I} = \mathbf{Y}(\mathbf{R})^+ \mathbf{A}, \tag{1}$$

using the pseudoinverse $(\cdot)^+$ of the system matrix $\mathbf{Y} \in \mathbb{R}^{N \times M}$. The resulting electrical power distribution was $E_j = I_j^2 R_j$, where j indicates the element-wise resistor selection. In turn, decoding process of the morphing basis into an electrodal voltage set is an inverse problem. Because the map is surjective-only, the optimization process has multiple global minima, leading the number of deterministic optimization unfavorable. As a result, a genetic algorithm (GA) was adopted to investigate one of the optimal solutions through intensive random search with multiple agents along the solution space. The cost function (J) was empirically designed as

$$J\left(\mathbf{W}, \mathbf{E}, \hat{\mathbf{E}}\right) = \mathbb{E}\left[\mathbf{W} \odot \left(\mathbf{E} - \hat{\mathbf{E}}\right)\right], \tag{2}$$

where the computation estimates the error between the output of the reference $\mathbf{E}$ and the estimate $\hat{\mathbf{E}}$ using the weight term $\mathbf{W}$ and Hadamard (element-wise) multiplication ($\odot$). $\mathbf{W} \in \mathbb{R}^M$ was designed to focus attention on the region of interest (ROI) in the actuation (sketched region in this work), expressed as

$$W_i = \begin{cases} \alpha, \text{ if } i^{th} \text{element is in ROI} \\ 1, \text{ otherwise,} \end{cases} \tag{3}$$

where $\alpha(>1)$ is an attention coefficient whose optimum value was empirically determined to be 3 in this work. The GA operation involves the sequential processes of selection, crossover, mutation, and replacement. Starting from a randomly initialized number of 5000 agents and 550 selections it proceeds to preserve only the agents having the best fitness. Crossover sorts two arbitrary agents and mutation randomly perturbs agents with constant probabilities of P = 0.3, 0.0018, respectively. The termination criterion is set at no progress for 30 iterations. The computation was performed by customized code using MATLAB (MathWorks, USA) and Python.

The resulting computation requires approximately 7.3 ms per iteration, and < 0.8 s for each morphing basis. Parallel computation can decode multiple morphing bases. The reconstruction performance was evaluated by comparison with two numerical approaches (the Levenberg-Marquardt algorithm and the linear pseudoinverse method; see Supplementary Note 7).

Resistive network imaging

The forward problem of RNI predicts the voltage measurements from the resistance distribution. Similar to the actuation algorithm, this relationship can be determined using an electrical network analysis. The measurement of RNI proceeds with multiple current injections and subsequent voltage measurements using a repetitive selection of electrode pairs for each (see Supplementary Fig. 25 for details about pair selection). This method of pair selection, referred to as the drive pattern, is a substantial specification for RNI measurements, affecting both reconstruction accuracy and frame rate. The ideal drive pattern, which recruits all possible combinations, is undesirable owing to the large number of sets (total measurements exceeding 10k). Therefore, the drive pattern was specifically designed based on spatial sensitivity analysis, resulting in a total of 1470 sequential pair-wise electrode recruitments (See Supplementary Note 8 for details of the drive pattern configuration).

A forward operator $F(\cdot)$ can be defined as

$$\mathbf{V} = F(\mathbf{R}), \tag{4}$$

where total L number of voltage measurements in the drive pattern are merged into a single vector, $\mathbf{V} \in \mathbb{R}^L$. Sensing with the RNI in turn involves the inverse problem of the forward relationship, which involves a variety of solving approaches. Among them, a deep-learning-based approach to electrical tomographic reconstruction was proposed to alleviate the problem of the trade-off between reconstruction accuracy and inference time in conventional numerical approaches. As an extension of our previous work, a sim-to-real transfer approach using a resistive network simulation was adopted (Supplementary Note 9). The dataset was synthesized by the forward simulation of the voltage response from the randomized resistance changes within the normalized range of 0–1.2, corresponding to the temperature change of 0–200 °C. The range beyond the operational range of sheet was imparted for generalization. Consequently, 400,000 data were collected for the training dataset. The model architecture was designed as three fully-connected layers with 308 neurons, with batch normalization, and a rectified linear unit (ReLU) activation function. The model was trained using the mean squared error loss function, ADAM optimization with a learning rate of 0.0001, mini-batch size of 256 and validation data split from 15% of the dataset. To account for measurement uncertainty in reality, additive Gaussian noise (standard deviation of 3 mV) was introduced at the initial stage of the training input. The training was carried out with Tensorflow 2.2.0 on a single graphics processing unit (GeForce Titan X, 12GB RAM; NVIDIA, USA).

The reconstruction performance was evaluated in comparison with two numerical approaches (One-step GN as a linear method, and Iterative GN as a nonlinear method, see Supplementary Note 9 for details in the reconstruction methods). To this end, an image error (root mean squared error, RMSE) was measured in the simulation, with respect to a reference input with varying resistance changes (see Supplementary Fig. 15 for the results).

Drive electronics

Embeddable electronics, composed of a microcontroller, circuit board, and power supply, drive the robotic sheet. A FPGA-based microcontroller (myRIO-1900 and LabVIEW software; National Instruments, USA) was used for operation owing to its compact size (13.07 × 8.27 × 1.31 cm) along with its fast, time-deterministic processing (>50 kHz; Analog reading, >1 MHz; digital control). The FPGA logic was constructed for the underlying circuit operation, whereas high-level data processing (including morphing basis recruitment, control trajectory generation, and deep learning model inference) was performed by the central processing unit of either the microcontroller or personal computer.

The electronic operation for electrothermal actuation involved allocating an appropriate voltage level to each electrode. To this end, a high current-tolerable 8:1 multiplexer IC (TMUX6208, withstanding maximum current of 300 mA; Texas Instruments, USA), which we refer to as Actuation MUX, provided voltage selections (± 15 V, ± 10 V, ± 5 V, ground, float) at each electrode. The digital control of all Actuation MUXs invites several independent digital commands (a total of 192; number of electrodes × 3). Sequential addressing using a memory buffer was implemented as an alternative. Specifically, a single master demultiplexer (192:1 and composed of six 32:1 demultiplexer ICs (ADG732; Analog Devices, USA)) sequentially stored the digital logic in the memory buffer attached to each digital port of the Actuation MUX (Quad NOR R-S Latch IC (CD4043BD; Texas Instruments, USA)). (See Supplementary Fig. 17a for the electronic circuit).

The RNI measurement involves the pairwise selection of the electrodes for both current injection and voltage measurement, accompanied by 64:1 multiplexing at each electrode selection, which we refer to as Sensing MUX. To this end, a sequential connection of one 4:1 multiplexer IC (ADG1404; Analog Devices, USA) with four 16:1 multiplexer ICs (ADG1406; Analog Devices, USA) was adopted to meet the requirements of low one-resistance (9.5 Ω) having high voltage tolerance (withstanding ± 15 V). (See Supplementary Fig. 17b for the electronic circuit).

Precise scheduling offers rapid operation of functionalities (Supplementary Fig. 16b). For actuation, the digital configuration lasts < 160 μs, and the heating pulse is injected for a portion of the fixed time period of 8 ms. The RNI measurement involves the repeat of the digitalized electrode selection process and corresponding voltage reading, lasting 4.5 μs and 5.6 μs, respectively, for a total of 14.85 ms for the proposed drive pattern. The ultrafast transition of the functionalities is performed using a single digital controller, lasting 275 ns.

Closed-loop temperature control

Temperature modulation is performed by proportional-integral (PI) control on each segmental morphing basis recruitment, which is a popular choice to address the thermal disturbance that exhibits a slow but persistent dynamical process. The gains for P and I control were empirically set as 0.4, and 0.009, respectively. The selection process for these gains is detailed via a transient response analysis (Supplementary Fig. 19). The saturation of the control variable was imposed on the temperature measurements to prevent overheating.

The experimental characterizations for the temperature control were performed with the following considerations. The frequency response was measured in response to harmonic inputs with varying frequencies. Because of the nonlinearity of the system dynamics, peak-to-peak and cross-correlation analyses were devised to measure the magnitude and phase, respectively. Cross-correlation estimates the lag at the best match between the reference and measured signals. Robustness against thermal disturbances was measured in response to artificial wind (exhibited using a commercial portable fan) and heat plates, both in a closed chamber.

Grasping

The robotic sheet was installed on a customized continuum manipulator, constructed using 3D-printed components, and driven by agonistic-antagonistic cable pulling (See Supplementary Fig. 26 for details of the manipulator). A quartz rod (diameter: 4 mm; height: 10 mm) was attached using silicone adhesive to mediate their interconnections. Electrical wires were hindered to the inner cavity of the manipulator. To protect objects from thermal damage, the structural neutralization temperature for this application was tuned to room temperature (26–30 °C). Objects were selected from those encountered in daily life (Petri dish, snack, wooden stick, sponge, and rubber mat).

Locomotion

The terrain for the sheet operation adopted a plastic plane (Polytetrafluoroethylene, PTFE; Sungjin, South Korea) colored by adhering to the bottom layer of a commercial white sheet. The sequential morphing intent for each locomotion was empirically designed based on the following considerations: (i) polyimide is more slippery than PDMS during frictional interactions with the terrain, (ii) a wider surface contact results in a larger friction force, and (iii) the cooling process is slower than heating. All the operations adopted a closed-loop temperature-control strategy.

Data availability

All data from this study can be found in the main text and Supplementary Information. Source data are provided with this paper.

Code availability

A training code for deep-learning-based resistive network imaging method is available from https://github.com/HyunkyuPark-biorobotics/FieldProgrammableRoboticFoldingSheet[61]. Other codes are available from the corresponding authors upon request.

References

1. Rus, D. & Tolley, M. T. Design, fabrication and control of soft robots. *Nature* **521**, 467–475 (2015).
2. Belke, C. H., Holdcroft, K., Sigrist, A. & Paik, J. Morphological flexibility in robotic systems through physical polygon meshing. *Nat. Mach. Intell.* **5**, 669–675 (2023).
3. Gardner, J. P. et al. The james webb space telescope. *Space Sci. Rev.* **123**, 485–606 (2006).
4. Kim, S.-J., Lee, D.-Y., Jung, G.-P. & Cho, K.-J. An origami-inspired, self-locking robotic arm that can be folded flat. *Sci. Robot* **3**, eaar2915 (2018).
5. Yan, W. et al. Origami-based integration of robots that sense, decide, and respond. *Nat. Commun.* **14**, 1553 (2023).
6. Shah, D. S. et al. A soft robot that adapts to environments through shape change. *Nat. Mach. Intell.* **3**, 51–59 (2021).
7. Lee, D.-Y., Kim, J.-K., Sohn, C.-Y., Heo, J.-M. & Cho, K.-J. High–load capacity origami transformable wheel. *Sci. Robot* **6**, eabe0201 (2021).
8. Zhang, C. et al. Plug & play origami modules with all-purpose deformation modes. *Nat. Commun.* **14**, 4329 (2023).
9. Oh, S. et al. 3D shape-morphing display enabled by electro-thermally responsive, stiffness-tunable liquid metal platform with stretchable electroluminescent device. *Adv. Funct. Mater.* **33**, 2214766 (2023).
10. Johnson, B. K. et al. A multifunctional soft robotic shape display with high-speed actuation, sensing, and control. *Nat. Commun.* **14**, 4516 (2023).
11. Xin, C. et al. Environmentally adaptive shape-morphing microrobots for localized cancer cell treatment. *ACS Nano* **15**, 18048–18059 (2021).
12. Hu, W., Lum, G. Z., Mastrangeli, M. & Sitti, M. Small-scale soft-bodied robot with multimodal locomotion. *Nature* **554**, 81–85 (2018).
13. Kim, Y., Yuk, H., Zhao, R., Chester, S. A. & Zhao, X. Printing ferromagnetic domains for untethered fast-transforming soft materials. *Nature* **558**, 274–279 (2018).
14. Ze, Q. et al. Soft robotic origami crawler. *Sci. Adv.* **8**, eabm7834 (2022).
15. Yi, S. et al. High-throughput fabrication of soft magneto-origami machines. *Nat. Commun.* **13**, 4177 (2022).
16. Yao, S., Cui, J., Cui, Z. & Zhu, Y. Soft electrothermal actuators using silver nanowire heaters. *Nanoscale* **9**, 3797–3805 (2017).
17. Sîrbu, I.-D. et al. Electrostatic actuators with constant force at low power loss using matched dielectrics. *Nat. Electron* **6**, 888–899 (2023).
18. Li, W. et al. An on-demand plant-based actuator created using conformable electrodes. *Nat. Electron* **4**, 134–142 (2021).
19. Kuenstler, A. S. et al. Blueprinting photothermal shape-morphing of liquid crystal elastomers. *Adv. Mater.* **32**, 2000609 (2020).
20. Han, B. et al. Plasmonic-assisted graphene oxide artificial muscles. *Adv. Mater.* **31**, 1806386 (2019).
21. Cangialosi, A. et al. DNA sequence–directed shape change of photopatterned hydrogels via high-degree swelling. *Science* **357**, 1126–1130 (2017).
22. Wehner, M. et al. An integrated design and fabrication strategy for entirely soft, autonomous robots. *Nature* **536**, 451–455 (2016).
23. Siéfert, E., Reyssat, E., Bico, J. & Roman, B. Bio-inspired pneumatic shape-morphing elastomers. *Nat. Mater.* **18**, 24–28 (2019).
24. Melancon, D., Gorissen, B., García-Mora, C. J., Hoberman, C. & Bertoldi, K. Multistable inflatable origami structures at the metre scale. *Nature* **592**, 545–550 (2021).
25. Jones, T. J., Jambon-Puillet, E., Marthelot, J. & Brun, P.-T. Bubble casting soft robotics. *Nature* **599**, 229–233 (2021).
26. Cui, J. et al. Nanomagnetic encoding of shape-morphing micromachines. *Nature* **575**, 164–168 (2019).
27. Hawkes, E. et al. Programmable matter by folding. *Proc. Natl Acad. Sci.* **107**, 12441–12445 (2010).
28. Li, G. et al. Self-powered soft robot in the Mariana Trench. *Nature* **591**, 66–71 (2021).
29. Hawkes, E. W., Blumenschein, L. H., Greer, J. D. & Okamura, A. M. A soft robot that navigates its environment through growth. *Sci. Robot* **2**, eaan3028 (2017).
30. Barbarino, S., Saavedra Flores, E. I., Ajaj, R. M., Dayyani, I. & Friswell, M. I. A review on shape memory alloys with applications to morphing aircraft. *Smart Mater. Struct.* **23**, 063001 (2014).
31. Tang, Y. et al. Wireless miniature magnetic phase-change soft actuators. *Adv. Mater.* **34**, 2204185 (2022).
32. Ford, M. J. et al. A multifunctional shape-morphing elastomer with liquid metal inclusions. *Proc. Natl Acad. Sci.* **116**, 21438–21444 (2019).
33. Roh, Y. et al. Vital signal sensing and manipulation of a microscale organ with a multifunctional soft gripper. *Sci. Robot* **6**, eabi6774 (2021).
34. Liu, Q. et al. Electronically configurable microscopic metasheet robots.*Nat. Mater.* **24**, 109–115 (2025).
35. Guseinov, R., McMahan, C., Pérez, J., Daraio, C. & Bickel, B. Programming temporal morphing of self-actuated shells. *Nat. Commun.* **11**, 237 (2020).
36. Boley, J. W. et al. Shape-shifting structured lattices via multimaterial 4D printing. *Proc. Natl Acad. Sci.* **116**, 20856–20862 (2019).
37. Liu, Y., Shaw, B., Dickey, M. D. & Genzer, J. Sequential self-folding of polymer sheets. *Sci. Adv.* **3**, e1602417 (2017).
38. Tian, Z. et al. Gaussian-preserved, non-volatile shape morphing in three-dimensional microstructures for dual-functional electronic devices. *Nat. Commun.* **12**, 509 (2021).
39. Rus, D. & Tolley, M. T. Design, fabrication and control of origami robots. *Nat. Rev. Mater.* **3**, 101–112 (2018).
40. Kohlmeyer, R. R. et al. Shape-reprogrammable polymers: encoding, erasing, and re-encoding. *Adv. Mater.* **26**, 8114–8119 (2014).
41. Chen, T., Pauly, M. & Reis, P. M. A reprogrammable mechanical metamaterial with stable memory. *Nature* **589**, 386–390 (2021).
42. Meeussen, A. S. & van Hecke, M. Multistable sheets with rewritable patterns for switchable shape-morphing. *Nature* **621**, 516–520 (2023).
43. Alapan, Y., Karacakol, A. C., Guzelhan, S. N., Isik, I. & Sitti, M. Reprogrammable shape morphing of magnetic soft machines. *Sci. Adv.* **6**, eabc6414 (2020).
44. Niu, D. et al. Reconfigurable shape-morphing flexible surfaces realized by individually addressable photoactuator arrays. *Smart Mater. Struct.* **30**, 125032 (2021).
45. Wang, J., Sotzing, M., Lee, M. & Chortos, A. Passively addressed robotic morphing surface (PARMS) based on machine learning. *Sci. Adv.* **9**, eadg8019 (2023).
46. Liu, K., Hacker, F. & Daraio, C. Robotic surfaces with reversible, spatiotemporal control for shape morphing and object manipulation. *Sci. Robot* **6**, eabf5116 (2021).
47. Bai, Y. et al. A dynamically reprogrammable surface with self-evolving shape morphing. *Nature* **609**, 701–708 (2022).
48. Ni, X. et al. Soft shape-programmable surfaces by fast electromagnetic actuation of liquid metal networks. *Nat. Commun.* **13**, 5576 (2022).

49. Benbernou, N. M., Demaine E. D., Demaine, M. L. Universal hinge patterns for folding orthogonal shapes. *Origami 5*. (Taylor & Francis Group, New York, 2011).
50. An, B., Beenbernou, N. M., Demaine, E. D. & Rus, D. L. Planning to fold multiple objects from a single self-folding sheet. *Robotica* **29**, 87–102 (2011).
51. An, B. & Rus, D. Designing and programming self-folding sheets. *Robot Auton. Syst.* **62**, 976–1001 (2014).
52. Adler, A. & Holder, D. Electrical impedance tomography. (CRC Press, 2021).
53. Park, H., Park, K., Mo, S. & Kim, J. Deep neural network based electrical impedance tomographic sensing methodology for large-area robotic tactile sensing. *IEEE Trans. Robot.* **37**, 1570–1583 (2021).
54. Shintake, J., Cacucciolo, V., Floreano, D. & Shea, H. Soft robotic grippers. *Adv. Mater.* **30**, 1707035 (2018).
55. Geim, A. K. et al. Microfabricated adhesive mimicking gecko foot-hair. *Nat. Mater.* **2**, 461–463 (2003).
56. Spielberg, A. et al. Learning-in-the-loop optimization: end-to-end control and co-design of soft robots through learned deep latent representations. *Adv. Neural Inf. Process Syst.* **32**, 8284–8294 (2019).
57. Ni, X. et al. 2D mechanical metamaterials with widely tunable unusual modes of thermal expansion. *Adv. Mater.* **31**, 1905405 (2019).
58. Liu, Y. et al. Fully inkjet-printed Ag_2Se flexible thermoelectric devices for sustainable power generation. *Nat. Commun.* **15**, 2141 (2024).
59. Kim, S. et al. Passive isothermal film with self-switchable radiative cooling-driven water sorption layer for arid climate applications. *Nat. Commun.* **15**, 8000 (2024).
60. Kumar, V. et al. Microengineered materials with self-healing features for soft robotics. *Adv. Intell. Syst.* **3**, 2100005 (2021).
61. Park, H. et al. Field-programmable robotic folding sheet. Github repository, https://doi.org/10.5281/zenodo.15497136 (2025).

Acknowledgments

This work was supported by a National Research Foundation of Korea (NRF) grant funded by the Korean government (MSIT) (RS-2021-NR059641) (J.K.) and the Korean government (MSIT, No. 2021R1A2C3008742) (I.P.).

Author contributions

H.P. and Y.J. contributed equally to this work. H.P. and Y.J. conceived the ideas. I.P. and J.K. supervised the project. H.P., Y.J., I.P., and J.K. wrote the manuscript. Y.J., J.C., J.A., and J.H.J. fabricated the samples. H.P. and Y.J. performed thermomechanical simulation. H.P. and Y.J. performed the material characterization experiments. H.P. constructed the programming framework, algorithms, and electronics. H.P. performed the fold-programmability experiments. H.P., Y.J., and W.K. performed the application demonstrations. All authors contributed to the analysis, discussion of results and preparation of the manuscript.

Competing interests

The authors declare no competing interests.

Additional information

Supplementary information The online version contains supplementary material available at https://doi.org/10.1038/s41467-025-61838-3.

Correspondence and requests for materials should be addressed to Inkyu Park or Jung Kim.

Peer review information *Nature Communications* thanks Suyi Li, Yuan-Fang Zhang, Byoungkwon An, and the other, anonymous, reviewer(s) for their contribution to the peer review of this work. A peer review file is available.

Reprints and permissions information is available at http://www.nature.com/reprints

Publisher's note Springer Nature remains neutral with regard to jurisdictional claims in published maps and institutional affiliations.

Open Access This article is licensed under a Creative Commons Attribution-NonCommercial-NoDerivatives 4.0 International License, which permits any non-commercial use, sharing, distribution and reproduction in any medium or format, as long as you give appropriate credit to the original author(s) and the source, provide a link to the Creative Commons licence, and indicate if you modified the licensed material. You do not have permission under this licence to share adapted material derived from this article or parts of it. The images or other third party material in this article are included in the article's Creative Commons licence, unless indicated otherwise in a credit line to the material. If material is not included in the article's Creative Commons licence and your intended use is not permitted by statutory regulation or exceeds the permitted use, you will need to obtain permission directly from the copyright holder. To view a copy of this licence, visit http://creativecommons.org/licenses/by-nc-nd/4.0/.

© The Author(s) 2025